

RESEARCH ARTICLE

10.1002/2015JD024528

This article is a companion to Wang *et al.* [2016] doi:10.1002/2015JD024526.

Key Points:

- The IR optimal estimation retrieval has been evaluated and compared with C6 MYD06 products
- The IR-based optical thickness and cloud top height retrievals agree well with C6 MYD06 and CALIOP products
- Obvious differences between the IR and the C6 MYD06 effective particle size are found

Correspondence to:

C. Wang,
chenxi@umd.edu

Citation:

Wang, C., S. Platnick, Z. Zhang, K. Meyer, G. Wind, and P. Yang (2016), Retrieval of ice cloud properties using an optimal estimation algorithm and MODIS infrared observations: 2. Retrieval evaluation, *J. Geophys. Res. Atmos.*, *121*, 5827–5845, doi:10.1002/2015JD024528.

Received 17 NOV 2015

Accepted 28 MAR 2016

Accepted article online 21 APR 2016

Published online 17 MAY 2016

Retrieval of ice cloud properties using an optimal estimation algorithm and MODIS infrared observations: 2. Retrieval evaluation

Chenxi Wang¹, Steven Platnick², Zhibo Zhang³, Kerry Meyer^{2,4}, Gala Wind², and Ping Yang⁵

¹Earth System Science Interdisciplinary Center, University of Maryland, College Park, Maryland, USA, ²NASA Goddard Space Flight Center, Greenbelt, Maryland, USA, ³Department of Physics, University of Maryland, Baltimore County, Baltimore, Maryland, USA, ⁴Goddard Earth Sciences Technology and Research, Universities Space Research Association, Columbia, Maryland, USA, ⁵Department of Atmospheric Sciences, Texas A&M University, College Station, Texas, USA

Abstract An infrared-based optimal estimation (OE-IR) algorithm for retrieving ice cloud properties is evaluated. Specifically, the implementation of the algorithm with MODerate resolution Imaging Spectroradiometer (MODIS) observations is assessed in comparison with the operational retrieval products from MODIS on the Aqua satellite (MYD06), Cloud-Aerosol Lidar with Orthogonal Polarization (CALIOP), and the Imaging Infrared Radiometer (IIR); the latter two instruments fly on the Cloud-Aerosol Lidar and Infrared Pathfinder Satellite Observation (CALIPSO) satellite in the Afternoon Constellation (A-Train) with Aqua. The results show that OE-IR cloud optical thickness (τ) and effective radius (r_{eff}) retrievals perform best for ice clouds having $0.5 < \tau < 7$ and $r_{\text{eff}} < 50 \mu\text{m}$. For global ice clouds, the averaged retrieval uncertainties of τ and r_{eff} are 19% and 33%, respectively. For optically thick ice clouds with τ larger than 10, however, the τ and r_{eff} retrieval uncertainties can exceed 30% and 50%, respectively. For ice cloud top height (h), the averaged global uncertainty is 0.48 km. Relatively large h uncertainty (e.g., > 1 km) occurs for $\tau < 0.5$. Analysis of 1 month of the OE-IR retrievals shows large τ and r_{eff} uncertainties in storm track regions and the southern oceans where convective clouds are frequently observed, as well as in high-latitude regions where temperature differences between the surface and cloud top are more ambiguous. Generally, comparisons between the OE-IR and the operational products show consistent τ and h retrievals. However, obvious differences between the OE-IR and the MODIS Collection 6 r_{eff} are found.

1. Introduction

In spite of a significant amount of effort by the atmospheric research community, an appropriate representation of cloud properties and processes in current climate models remains one of the largest sources of uncertainty in estimating the Earth-atmosphere energy budget and in predicting climate changes (Boucher *et al.* [2013] IPCC report). Waliser *et al.* [2009] reported significant discrepancies of global averaged ice water path and corresponding spatial distributions among climate models; Li *et al.* [2008] reported large intermodel differences of global liquid water path. Although satellite sensors have monitored global clouds for decades, observational constraints from current satellite-based instruments are nevertheless limited [Holl *et al.*, 2013], in part due to ongoing challenges in collectively using the broad suite of current satellite retrieval products [Eliasson *et al.*, 2011]. During the past several decades, numerous cloud retrieval algorithms have been developed and implemented with observations made by various satellite instruments [e.g., Smith and Platt, 1978; Nakajima and King, 1990; Parol *et al.*, 1991; Chepfer *et al.*, 1998; Platnick *et al.*, 2003; Menzel *et al.*, 2008; Austin *et al.*, 2009; Minnis *et al.*, 2011; Garnier *et al.*, 2012, 2013; Kahn *et al.*, 2014; Heidinger *et al.*, 2015]. These retrieval algorithms, developed for passive or active sensors and relying on different spectral channels, have different strengths and weaknesses in a wide variety of atmospheric scenarios. For example, passive sensors detect solar (or thermal) radiation reflected (emitted) by clouds. Algorithms based on solar radiation can be applied to daytime conditions only, whereas terrestrial infrared (IR)-based algorithms are independent of solar geometry and therefore can be applied to both daytime and nighttime. Meanwhile, due to the strong absorption by cloud particles in the IR spectrum, it has been recognized that IR-based algorithms have substantial advantages in retrieving optically thin cloud properties, whereas solar reflection-based algorithms are more suitable for optically thicker clouds [Baran and Francis, 2004; Cooper and Garrett, 2010; Wang *et al.*, 2011]. Different from passive sensors, active sensors (e.g., lidar and radar) emit pulses of radiation and measure cloud reflection (or emission) signals. With an active sensor, it is feasible to obtain vertical profiles of atmospheric columns with desirable resolutions.

However, observations from active sensors are limited to a fixed viewing angle and are therefore collected only along a narrow satellite track and may not have inherent radiative property information that can be attributed directly to passive observations.

In addition to the inherent strengths and weaknesses of the different sensors mentioned above, differences in the cloud and radiative transfer models used in retrieval algorithms also pose a challenge for combining and comparing various satellite-based retrieval products. For both passive and active sensors, measurements vary with cloud microphysical (e.g., cloud particle size and habit distributions) and macrophysical (e.g., cloud water path, cloud physical thickness, and height) properties. As it is impossible to simultaneously infer all of these cloud properties from a unique sensor, numerous assumptions have to be made in the retrieval algorithms. However, different cloud forward model assumptions between different retrievals make it difficult to compare retrieval products directly. Furthermore, inaccurate assumptions lead to retrieval uncertainties and biases, which are difficult to estimate. For these reasons, extensive effort has been devoted to understand retrieval differences among different sensors and algorithms [e.g., *Zhang et al.*, 2009; *Eliasson et al.*, 2013; *Lebsock and Su*, 2014]. For example, *Zhang et al.* [2009] found substantial differences between the MODerate resolution Imaging Spectroradiometer (MODIS) Collection 5 (C5) and the POLarization and Directionality of the Earth's Reflectances (POLDER) τ retrievals, even though both products are based on observations in the visible, near infrared, and shortwave infrared (VNIR/SWIR) channels. One of the major reasons is that the ice crystal habits assumed in the two retrieval algorithms are different. *Wang et al.* [2011] also reported systematic ice cloud τ retrieval differences between the MODIS C5 VNIR/SWIR algorithm and an IR-based algorithm, although the same ice crystal habits are assumed in each. Thus, retrieval differences between different algorithms can sometimes be reduced simply by improving the cloud forward model assumptions. For example, *Holz et al.* [2015] found that the use of aggregates of solid hexagonal columns [*Yang et al.*, 2013] with severely roughened surfaces significantly decreased the discrepancy between τ retrievals from the MODIS VNIR/SWIR algorithm and those from the Cloud-Aerosol Lidar with Orthogonal Polarization (CALIOP) and a MODIS IR-based algorithm for optically thin ice clouds; *Cole et al.* [2013] showed that the severely roughened ice crystals provide the best agreement between simulated and observed polarized reflectance using observations from PARASOL (Polarization and Anisotropy of Reflectances for Atmospheric Sciences coupled with Observations from a Lidar). These findings led to the decision to use the severely roughened column aggregate in the latest MODIS Collection 6 (C6) operational cloud retrieval algorithm (this crystal shape is hereafter referred to as the MODIS C6 habit).

While recent advances have been made, further effort is required to improve the current cloud retrieval algorithms with consistent and rectified models. As discussed above, agreement between cloud retrievals from different sensors, or from techniques using different spectral information, assuming a consistent ice crystal model can indicate the validity of the model or the robustness of a retrieval algorithm given that ice crystal optical properties significantly vary in different spectral regions; note that in some cases, for instance clouds having vertical ice crystal size distribution heterogeneity, retrieval disagreement may in fact be expected and therefore can also indicate model or retrieval algorithm validity. Thus, retrieval comparisons that yield improved models and algorithms, or that enhance our understanding of retrieval differences and uncertainties, offer an advancement toward the ultimate goal of establishing a consistent multisensor global cloud record. As part of this effort, we first evaluate an IR-based optimal estimation (OE-IR) ice cloud retrieval algorithm, introduced in Part 1 of this study, that is designed for MODIS-like multispectral imagers. MODIS, flying on the NASA Aqua and Terra satellites, has monitored global ice clouds for more than 13 years [*Barnes et al.*, 1998; *King et al.*, 2013], though the τ and effective particle radius (r_{eff}) retrievals are inherently daytime only since they rely on VNIR/SWIR reflectance measurements. Moreover, the possibility of combining the OE-IR retrieval, which can be applied in both daytime and nighttime, with the daytime-only MODIS C6 VNIR/SWIR retrieval (MOD06 and MYD06 for Terra and Aqua MODIS, respectively; though both algorithms are identical, only the MYD06 datafile [*Platnick et al.*, 2015] will be referred to here as all MODIS data are obtained from Aqua) [*Platnick et al.*, 2003, 2013] is explored; such a combination can provide Sun-synchronous daytime and nighttime cloud property retrievals for thin cirrus to moderately optically thick ice clouds. The OE-IR algorithm uses the same spectral channels in both daytime and nighttime and is less sensitive to the location of the Sun. Based on previous studies [e.g., *Holz et al.*, 2015], we select the same ice crystal habit model as is used in C6 MYD06 and take ice crystal habit uncertainty into account (discussed in Part 1). Therefore, it is expected that the C6 MYD06 ice cloud products and the OE-IR retrievals are

Table 1. Reference Ice Cloud Properties Used in the Synthetic Retrieval Analysis

	Variable Names	Notes
Reference ice cloud properties	Cloud optical thickness	0.1, 0.3, 0.5, 0.75, 1, 1.5, 2, 3, 5, 10
	Effective radius (μm)	5, 7.5, 10, 12.5, 15, 20, 25, 30, 40, 50
	Cloud top height (km)	5, 7.5, 10, 12.5, 15
Model parameter (errors)	Surface temperature (K)	294.2 (0.5)
	Surface emissivity	0.98 (0.01)
	Temperature profile	Midlatitude profile (1 K)
	Water vapor profile	Midlatitude profile (15%)

comparable if both VNIR/SWIR and IR signals are sufficiently sensitive to cloud properties and that cloud spatial heterogeneity does not bias the retrievals in systematically different ways. Such combined cloud retrievals will improve our understanding of ice cloud radiative models and help validate radiatively important ice cloud processes in models. While the OE-IR results shown here are exclusively from MODIS, the algorithm can be also applied to other MODIS-like instruments that have similar IR channels such as the future GOES-R Advanced Baseline Imager (ABI) [Schmit *et al.*, 2005], the Spinning Enhanced Visible and Infrared Imager (SEVIRI) [Aminou, 2002] on Meteosat Second Generation satellites, and hyperspectral resolution sensors such as the Cross-track Infrared Sounder (CrIS) [Han *et al.*, 2013] and Atmospheric Infrared Sounder (AIRS) [Aumann *et al.*, 2003].

This paper is organized as follows: section 2 discusses the OE-IR retrieval based on synthetic observations simulated with radiative transfer models that are perturbed with specified uncertainties. In section 3, we evaluate the pixel level OE-IR retrievals for a selected case study by comparing with the C6 MYD06 products and lidar and IR retrievals from the Cloud-Aerosol Lidar and Infrared Pathfinder Satellite Observations (CALIPSO). Furthermore, global OE-IR “Level-3” monthly aggregations are produced on a $1^\circ \times 1^\circ$ grid and are compared with the MODIS products in section 4. Discussion and conclusions are given in section 5.

2. Retrieval Algorithm Evaluation

To evaluate the performance of the OE-IR algorithm, we first implement the retrievals using synthetic MODIS observations. The simulations couple two rigorous radiative transfer models: the Line-by-Line Radiative Transfer Model (LBLRTM) [Clough *et al.*, 2005] and the DIScrete Ordinate Radiative Transfer algorithm (DISORT) [Stamnes *et al.*, 1988]. A set of ice cloud properties (τ , r_{eff} , and h) is used as the reference (listed in Table 1); the physical thickness of the simulated ice cloud is fixed at 1 km. A standard midlatitude summer profile [McClatchey *et al.*, 1972] is assumed for the atmosphere, and the surface is assumed to be Lambertian with temperature 294.2 K and emissivity 0.98. Up to 100,000 retrievals are conducted for each combination of ice cloud properties. Specifically, the “observations” are perturbed 100,000 times by adding independent Gaussian errors in 10 MODIS IR channels (3.8, 6.8, 7.3, 8.5, 11, 12, 13.3, 13.6, 13.9, and 14.2 μm) with standard deviation 0.1 K. Ancillary parameters, such as the air and surface temperatures, surface emissivity, and water vapor concentrations are also perturbed based on a Gaussian distribution. Standard deviations of the model parameter errors are listed in Table 1. Uncertainties for different types of physical variables (e.g., the air temperature and surface emissivity) are assumed to be independent, though air temperature and water vapor concentration uncertainties on different levels are vertically correlated. More details about the vertical correlation of the air temperature and water vapor profiles can be found in Part 1 of this study. Figure 1 shows τ and r_{eff} retrievals and corresponding uncertainties at two different altitudes. The intersection of each solid cross indicates the averaged retrieval using the 100,000 perturbed ancillary parameters and observations. The solid horizontal and vertical error bars indicate standard deviations of the 100,000 τ and r_{eff} retrievals, respectively. All four types of uncertainties (measurement uncertainty, fast radiative transfer model uncertainty, model parameter uncertainty, and ice crystal habit uncertainty) discussed in Part 1 are included. The dashed horizontal and vertical lines indicate the locations of the reference ice cloud properties. For a wide range of reference τ (0.3–5), no obvious retrieval bias is found for both τ and r_{eff} . However, τ and r_{eff} retrieval biases appear when the reference τ decreases to smaller than 0.3 or increases to greater than 5. We assume that the cloud physical thickness (1 km) is known without error. Figure 2 shows the τ and h retrievals and corresponding uncertainties at two reference r_{eff} values; here r_{eff} is assumed to be

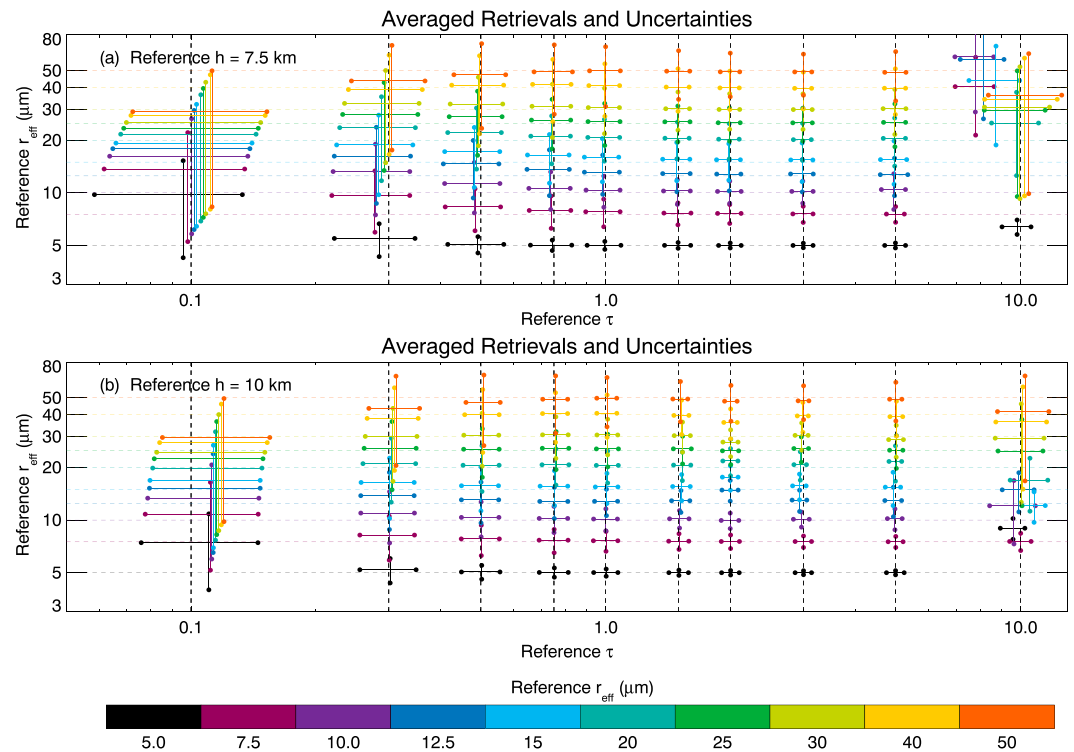


Figure 1. Averaged ice cloud properties and corresponding uncertainties inferred from synthetic observations simulated using reference ice cloud properties and 100,000 perturbed midlatitude summer atmospheric profiles. The different colors indicate different reference r_{eff} values. The solid vertical and horizontal bars indicate the averaged r_{eff} and τ retrieval uncertainties, respectively. The averaged retrievals are located at the intersections of the solid bars. The reference cloud properties are located at the intersections of the dashed horizontal and vertical lines. Cloud top height of (a) 7.5 and (b) 10 km.

homogeneously distributed in the vertical. For optically thin clouds ($\tau < 0.3$), obvious biases and uncertainties can be found for both τ and h retrievals. Both retrieval bias and uncertainty of h decrease with the increase of τ . An interesting feature is that the OE-IR retrieval tends to underestimate (overestimate) cloud top height if the ice cloud top is higher (lower) than 12 km (7 km). For the lower ice cloud, the h retrieval bias decreases with the increase of τ . However, a negative bias still exists for the high ice cloud even if $\tau > 5$. Further investigation is required to understand this bias. Figure 3 shows the corresponding retrieval cost function of Figure 1. The value of the cost function describes the difference between model simulations using retrieved cloud properties and the synthetic observations (see definition in Part 1). In the present OE-IR method using m observations, the retrieval is considered to converge to a reasonable solution if the cost function is comparable with or smaller than m (see equation (7) in Part 1). In Figures 1–3, we find that most retrievals have good qualities (cost function < 10) and the differences between the retrieved and reference values are generally smaller than the corresponding 1σ error bars. However, large cost functions and/or large biases can be found for a few cases with $\tau = 10$. For example, the red (cost function > 20) and orange dots (cost function > 10) in Figure 3 result from the large r_{eff} discrepancies between the retrievals and references. Meanwhile, large r_{eff} retrieval biases are also found even if the cost function values are small (e.g., cost function < 3), suggesting that local minimums are found during these retrievals. The sensitivity of IR observations to r_{eff} decreases rapidly if the cloud becomes optically thicker, leading to a larger r_{eff} retrieval uncertainty. Therefore, both the cost function and retrieval uncertainties should be considered when determining retrieval quality.

3. Case Studies

In this section, we apply the OE-IR ice cloud retrievals to an Aqua MODIS oceanic granule from May 2012 and compare the results for overcast ice cloud pixels with the C6 MYD06 cloud products [Platnick et al., 2015]. Partly cloudy pixels reported in the C6 MYD06 [Platnick et al., 2015] are not considered in this study.

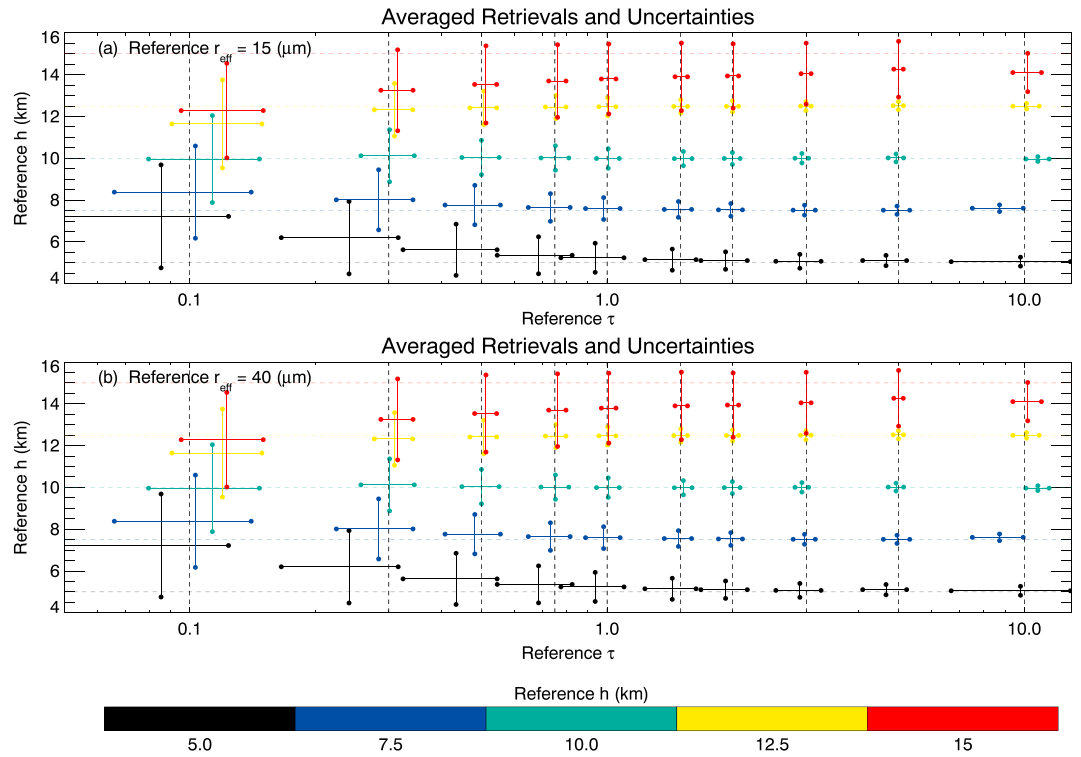


Figure 2. Same as Figure 1 but with different colors indicating different reference cloud top heights. Cloud effective radii of (a) 15 and (b) 40 μm .

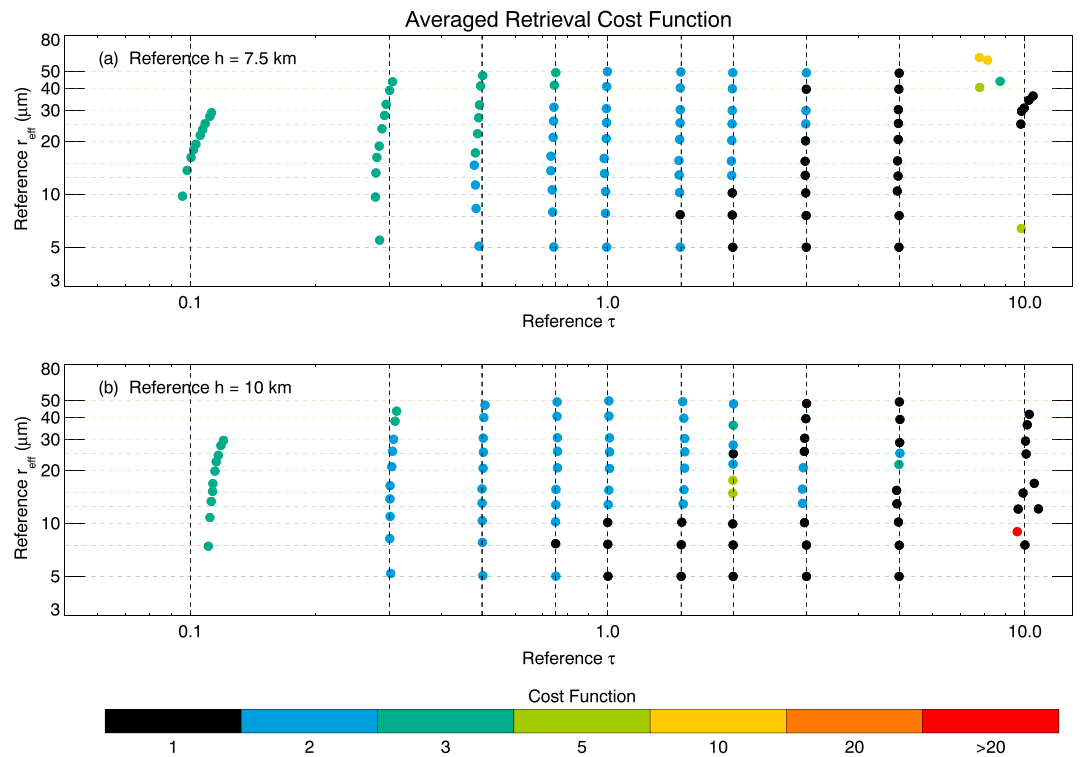


Figure 3. Averaged retrieval cost function values derived from the retrievals shown in Figure 1. The location of each dot indicates the averaged retrieved cloud properties (i.e., the intersection of the solid horizontal and vertical bars shown in Figure 1), while the color indicates averaged cost function magnitude. Cloud top height of (a) 7.5 and (b) 10 km.

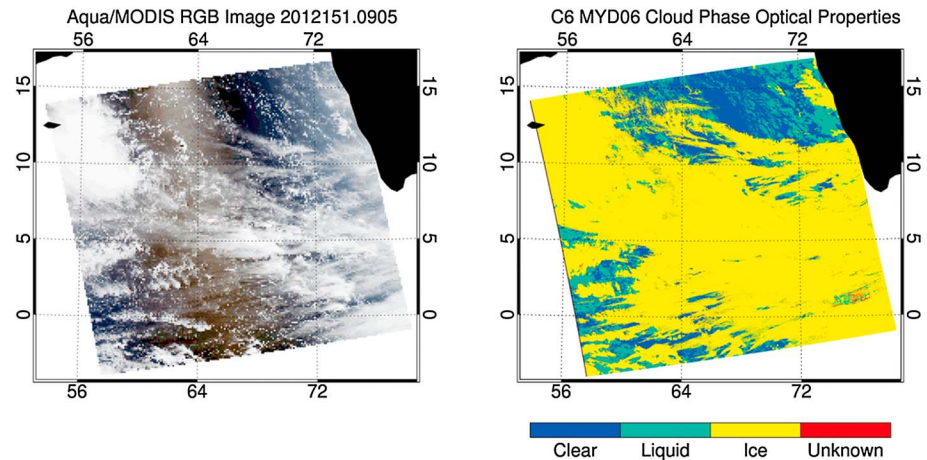


Figure 4. (left) A RGB (red: 640 nm; green: 550 nm; blue: 465 nm) image of an Aqua/MODIS daytime granule (30 May 2012, 0905 UTC) over the Indian Ocean. (right) The corresponding MODIS Cloud_Phase_Optical_Properties data set from C6 MYD06.

As previously discussed, MYD06 uses VNIR/SWIR reflectances to derive τ and r_{eff} ; thus, comparisons of τ and r_{eff} are only available during the daytime (defined as solar zenith angle $< 81.4^\circ$ for MYD06). The C6 MYD06 reports three independent r_{eff} retrieved using a typically VNIR channel along with the 1.6 or 2.1 μm SWIR channels or a midwave infrared (MWIR) 3.7 μm channel [Platnick *et al.*, 2015]; in this study, only the 2.1 μm -derived r_{eff} is used for comparison as it has been reported as the standard r_{eff} product in previous collections. Because C6 MYD06 uses the IR-based CO_2 slicing and IR window techniques for cloud top height retrievals at 1 km resolution [Baum *et al.*, 2012], h comparisons are available for both daytime and nighttime. In addition to MYD06, collocated lidar and IR retrieval products from CALIPSO are used for further evaluation. CALIOP [Winker *et al.*, 2010], measuring the nadir-backscattered signal at 532 and 1064 nm, is sensitive to optically thin scattering media such as cirrus and atmospheric aerosols and therefore provides a reliable reference for the physical cirrus top height, which may be substantially higher than the radiative height from IR observations [Kahn *et al.*, 2008; Holz *et al.*, 2008]. However, because the lidar signal is attenuated quickly when the cloud becomes optically thick, the CALIOP τ has an upper boundary of approximately 3. The Imaging Infrared Radiometer (IIR), which observes a narrow swath along the CALIPSO track, has three IR window channels located at 8.7, 10.6, and 12.1 μm , similar to MODIS channels 29, 31, and 32 (8.5, 11.0, and 12.0 μm). The IIR standard products include cloud absorption optical thickness at 12 μm and effective particle size. A scale factor of 2.25 is used to convert the IIR absorption optical thickness to the visible extinction optical thickness following previous studies [Garnier *et al.*, 2012].

Figure 4 (left) shows the true color RGB (red 640 nm, green 550 nm, and blue 465 nm) of an Aqua MODIS daytime granule (30 May 2012, 0905UTC) over the Indian Ocean. Figure 4 (right) shows the cloud phase used in the MYD06 cloud optical retrievals, suggesting that a large fraction of this granule is ice clouds (yellow). Except for some optically thick ice clouds in the top left corner, most of the ice clouds appear to be cirrus and have a fibrous appearance. Although we have used the multilayer cloud tests reported in the MYD06 data file (i.e., Cloud_Multi_Layer_Flag and Quality_Assurance_1km) to eliminate multilayer cloud cases [Wind *et al.*, 2010; Platnick *et al.*, 2015], it can be expected that some liquid cloud pixels exist in the top right and bottom left corners, and some cirrus pixels are likely multilayer scenes with underlying lower level liquid clouds.

Figure 5 shows retrieval comparisons between C6 MYD06 and OE-IR. The red line in each panel of Figure 5 indicates the location of the CALIPSO ground track. For cloud optical thickness τ (Figure 5, left column), the two products have similar patterns. Specifically, the two retrievals are consistent with each other for moderately optically thick ice cloud ($0.5 < \tau < 7$). However, the OE-IR τ retrievals are systematically smaller than MYD06 for optically thin cirrus with τ smaller than 0.5 (e.g., the edge of cirrus). The OE-IR retrieved τ has an upper limit at 12, while the MYD06 τ has an upper limit at 150, thus the appearance of smaller OE-IR τ when MYD06 τ is larger than 12. Retrieval uncertainties are shown in the third row. Measurement uncertainties in

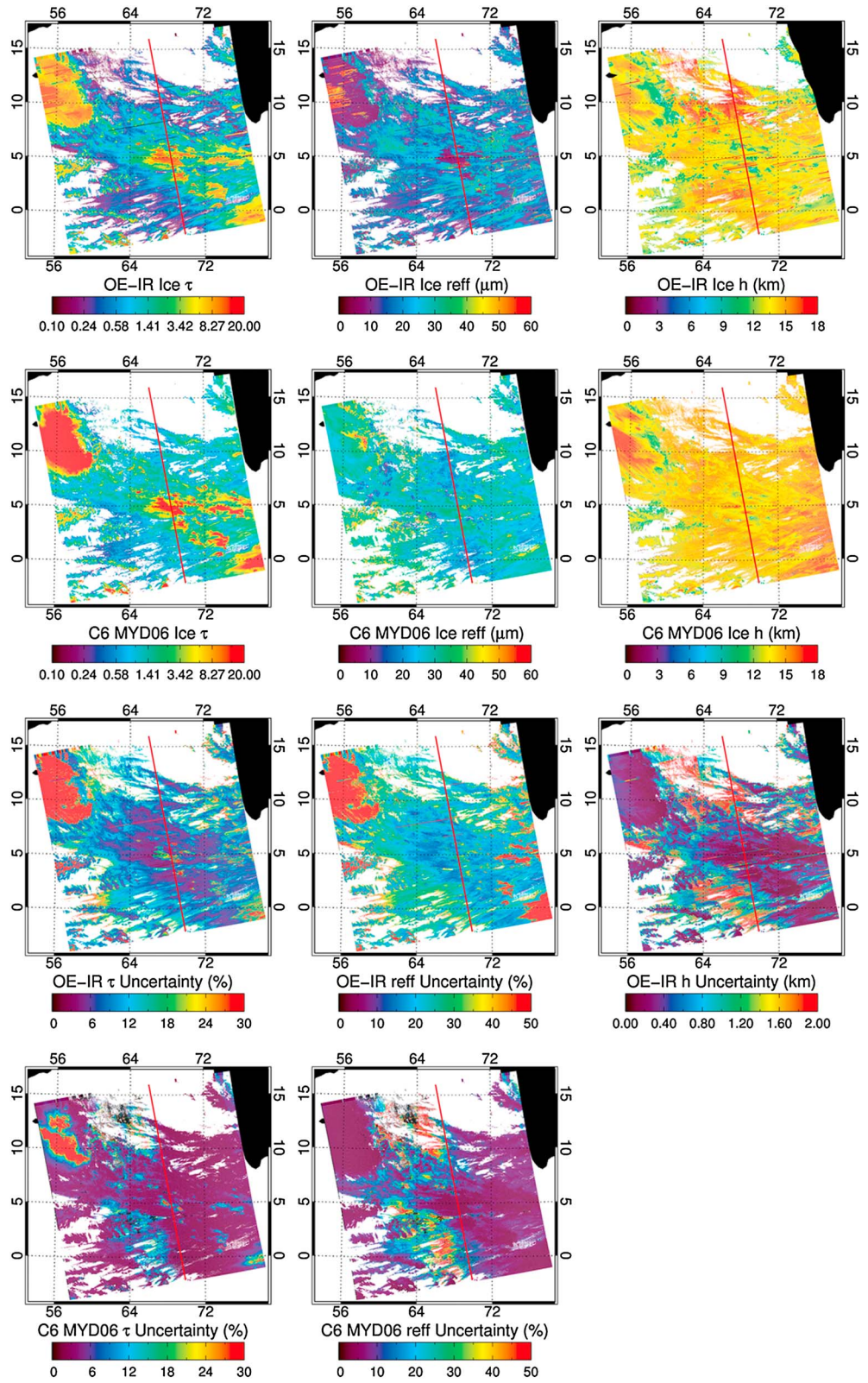


Figure 5. Retrieval comparisons of (left column) τ , (middle column) r_{eff} , and (right column) h between the OE-IR (first row) and the C6 MYD06 products (second row) for the Aqua MODIS daytime granule of Figure 4. The third and fourth rows show the corresponding retrieval uncertainties for the OE-IR and C6 MYD06, respectively. The red line in each panel indicates the CALIPSO ground track.

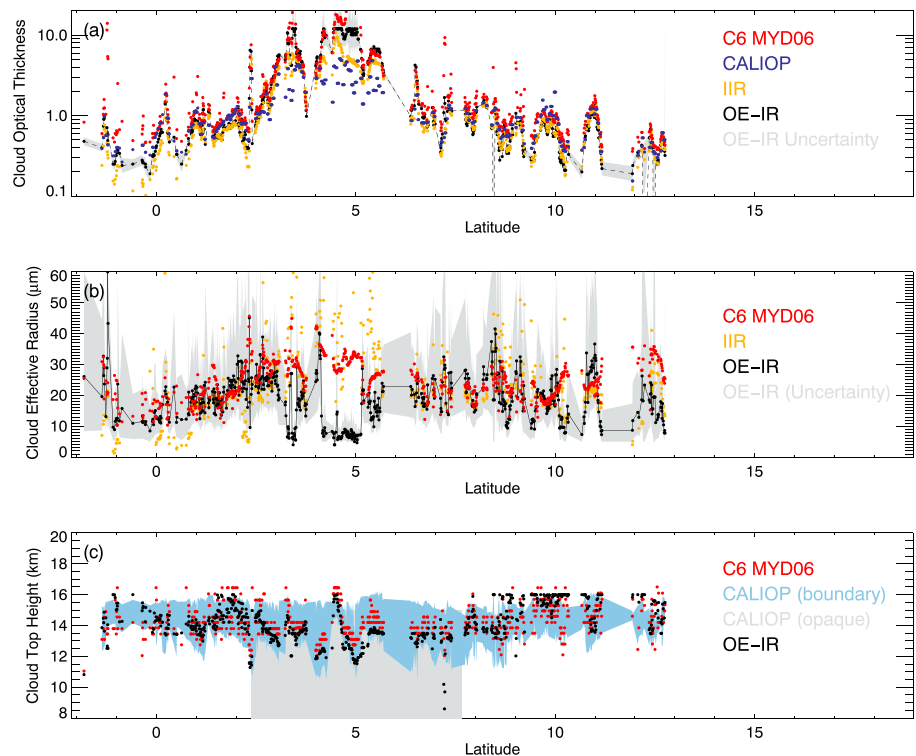


Figure 6. Retrieval comparisons of (a) τ , (b) r_{eff} , and (c) h along the CALIPSO track within the MODIS granule of Figures 4 and 5. The gray shaded areas in Figures 6a and 6b show the OE-IR τ and r_{eff} uncertainties, respectively. The light blue and gray shaded areas in Figure 6c indicate the CALIOP detected cloud layer boundaries and the locations where cloud are probably opaque (CALIOP $\tau > 2.5$), respectively.

brightness temperatures are extracted from the C6 MYD021KM product, and ancillary data set uncertainties are the same as those listed in Table 1 for oceanic cloud retrievals; for ice cloud retrievals over land, we assume a 2.0 K surface temperature uncertainty and a 0.03 surface emissivity uncertainty. The OE-IR τ retrievals have largest uncertainties for optically thick clouds ($\tau > 10$) and moderately large uncertainties for very thin cirrus ($\tau < 0.3$). The smallest τ retrieval uncertainty occurs when ice cloud τ is in the range between 1 and 7. Unlike τ , r_{eff} retrieval comparisons are complicated (middle column). The MYD06 r_{eff} values are generally larger than the OE-IR, and the spatial patterns of the MYD06 r_{eff} are different from their OE-IR counterpart. It is important to note that the OE-IR tends to retrieve extremely small r_{eff} if τ is large. Some large r_{eff} values are also found in the large τ regions (e.g., $r_{\text{eff}} > 50 \mu\text{m}$), suggesting that the OE-IR r_{eff} retrievals may not be stable if τ is too large. This feature is discussed in section 2. Since the OE-IR r_{eff} retrieval has large uncertainty and bias when τ exceeds 10 (see Figures in section 2), we recommend that the size retrieval should not be used in these cases. The cloud top height retrievals from the two products are similar (right column). The OE-IR h values are slightly lower than MYD06, which may be caused by the inclusion of MODIS water vapor channels in the OE-IR retrieval algorithm. The OE-IR h retrieval uncertainty reaches a minimum when the cloud is optically thick; the retrieval becomes more uncertain when the cloud is optically thin. The C6 MYD06 also provides uncertainties for τ and r_{eff} , which are shown in the bottom panels of Figure 5. The VNIR/SWIR 2.1 μm based retrieval has relatively large τ uncertainties ($\sim 30\%$) for clouds with $\tau > 20$, and large r_{eff} uncertainties for clouds with $\tau < 1$. The C6 MYD06 τ and r_{eff} uncertainties are systematically smaller than the OE-IR. A possible reason is that the ice crystal habit uncertainty, which is an important component of the OE-IR retrieval (see Part 1) and is expected to be a large source of uncertainty in solar-based retrievals [e.g., Zhang et al., 2009; Baum et al., 2014; Heidinger et al., 2015; Holz et al., 2015], is not considered in the C6 MYD06 product. In addition, a small fraction of ice cloud pixels are over land (upper right corner of this granule). Since larger uncertainties are given for ancillary data over land, the OE-IR retrieval uncertainties of these cloud pixels are slightly higher than oceanic cloud pixels with similar cloud properties.

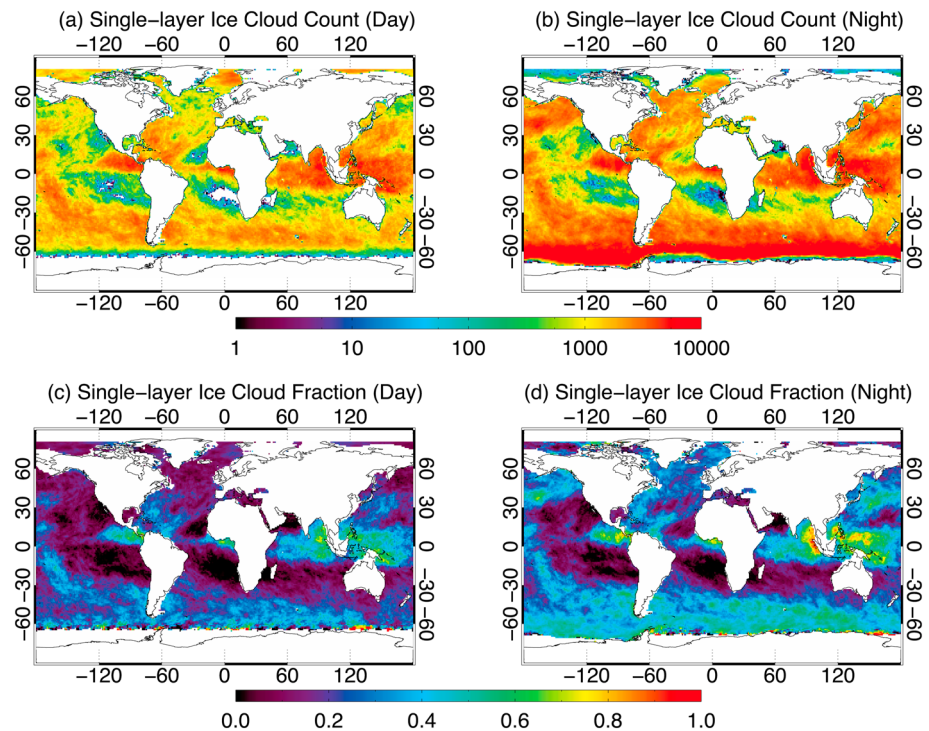


Figure 7. (a, b) Number of ice cloud pixels and (c, d) corresponding ice cloud fractions, sampled during the daytime (Figures 7a and 7c) and nighttime (Figures 7b and 7d) for May 2012. The change of cloud properties could be real or be caused by the different cloud phase products used in the daytime and nighttime.

Along-track comparisons with the CALIPSO lidar and IR products are shown in Figure 6; the different retrievals are color coded as indicated in each plot. Only single-layered ice clouds according to the CALIPSO lidar are used for comparison. The gray shaded areas in Figures 6a and 6b indicate corresponding uncertainties of the OE-IR retrievals. For ice cloud τ , all four retrievals capture the variation of the ice cloud. The OE-IR, IIR, and CALIOP τ near the equator ($2^{\circ}\text{S} \sim 2^{\circ}\text{N}$) have similar values around 0.3–0.5, which are smaller than the MYD06 C6 τ . All τ retrievals reach their maximum near $3\text{--}6^{\circ}\text{N}$, where a thicker ice cloud is observed. In this case, the IIR and CALIOP τ become saturated quickly at roughly 5 and 3, respectively. However, the MYD06 and OE-IR τ increase up to more than 10. Figure 6b shows comparisons of the r_{eff} retrievals. The largest discrepancy among the MYD06, IIR, and OE-IR occurs when the cloud is optically thick. Specifically, the OE-IR retrieved r_{eff} values reach the lower limit defined in the retrieval algorithm ($5\ \mu\text{m}$), which are expected to have the largest biases and should not be used. However, the C6 MYD06, IIR, and OE-IR r_{eff} retrievals are comparable if τ is smaller than 7. The cloud top height comparison is shown in Figure 6c. Also included are the CALIOP ice cloud bottom boundaries, though it is important to emphasize that the CALIOP-detected lower boundary may be higher than the real ice cloud bottom if the lidar signal attenuates and cannot penetrate the whole cloud layer. Both the MYD06 and OE-IR retrieved h are located within the CALIOP ice cloud boundaries. Meanwhile, the OE-IR-retrieved h is closer to the CALIOP cloud top for optically thin cirrus and tends to the limit of CALIOP penetration depth within the ($\tau \approx 3$) cloud bottom for optically thick clouds. In this study, a fixed cloud physical thickness (1 km) is used in the OE-IR algorithm regardless of how optically thick the cloud is. Therefore, the retrieved h , which is an effective radiative cloud top height, is expected to be lower than the actual radiative cloud top height if the cloud is physically thicker than 1 km.

4. Comparing Global Monthly Statistics

We apply an aggregation strategy to generate daily (not shown) and monthly Level-3 retrieval products using the OE-IR pixel level (Level 2) retrievals for May 2012 and compare with a similar aggregation of the C6 MYD06 products; note that the global monthly MYD06 aggregation is not the operational archived global gridded product (MYD08) but is produced by the same algorithm used for the OE-IR aggregation. Only deep

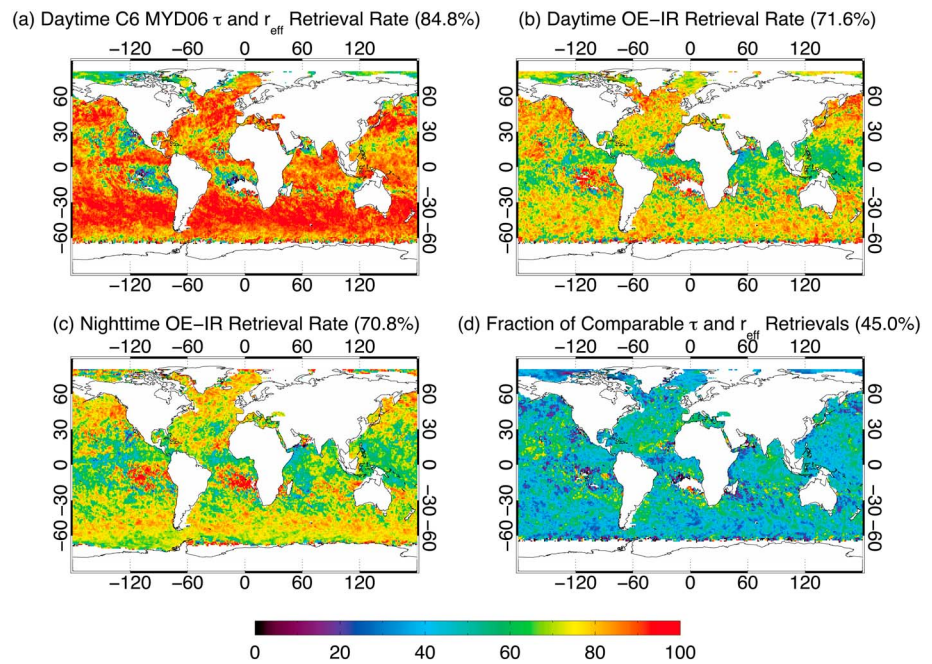


Figure 8. (a and b) Successful retrieval τ and r_{eff} rates of the C6 MYD06 and the OE-IR algorithms for May 2012 daytime ice clouds; (c) successful retrieval τ and r_{eff} rate of the OE-IR algorithm for nighttime ice clouds; and (d) fraction ice cloud pixels with comparable τ and r_{eff} retrieval subset. Definitions of successful and comparable retrievals are given in Table 2. Numbers shown in the parentheses are retrieval rates (fractions) for global ice clouds.

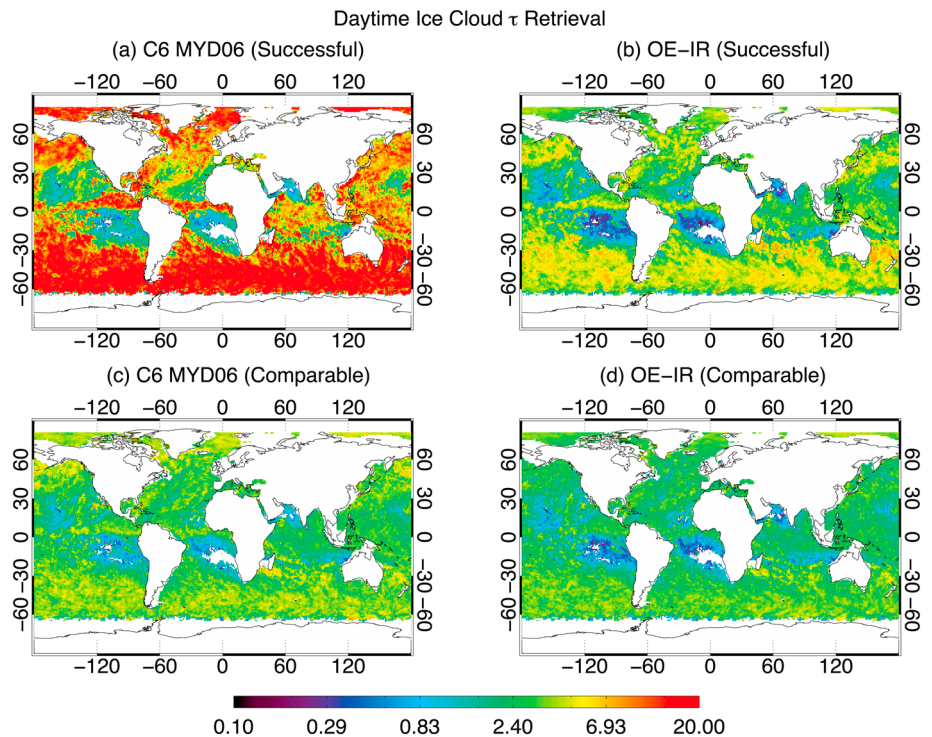


Figure 9. Comparisons of monthly daytime τ retrievals between the C6 MYD06 and OE-IR. (a, b) Successful τ retrievals; (c, d) comparable τ retrievals (see text for definition).

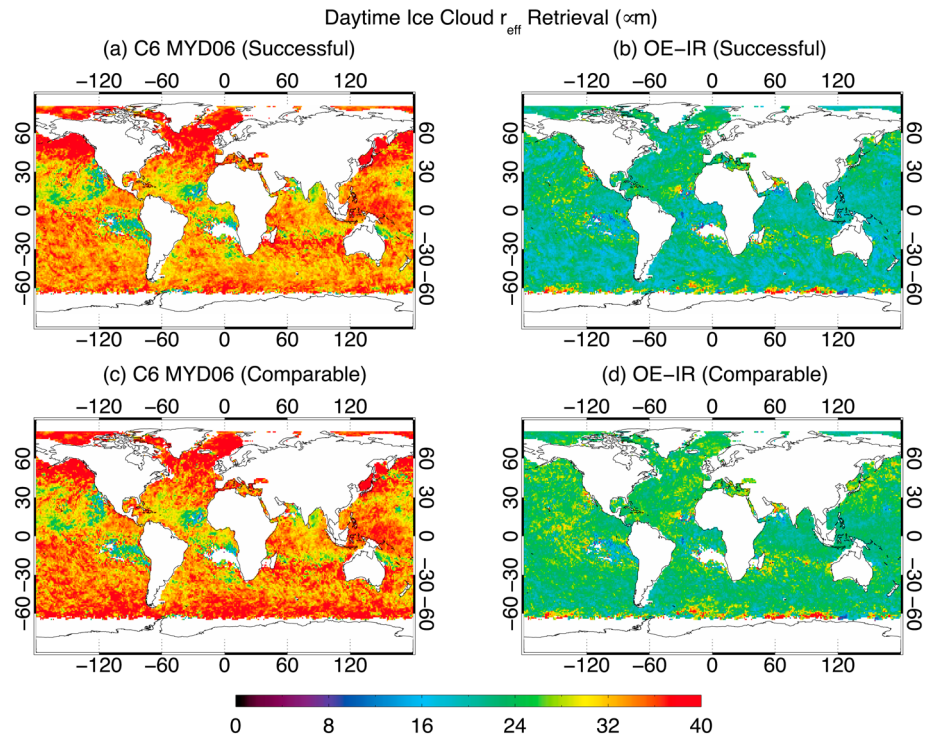


Figure 10. Comparisons of monthly daytime r_{eff} retrievals between the C6 MYD06 and OE-IR. (a, b) Successful r_{eff} retrievals; (c, d) comparable r_{eff} retrievals.

ocean pixels without sea ice (Land/Sea Mask = 7 in the MYD03 geolocation product and Snow/Ice Mask = 1 in MODIS cloud mask product) are used in the present aggregations for better comparison. High-latitude regions (80~90°N/S) are not included in order to avoid relatively large uncertainties of the VNIR/SWIR- and MWIR-based retrieval products. Ice cloud pixels are determined using the two cloud phase products available in C6 MYD06. The first product, reported in Cloud_Phase_Optical_Properties and denoted here as f_1 , is the daytime-only phase used in the MYD06 cloud optical retrievals, which for C6 is derived from thresholds on cloud top temperature and spectral r_{eff} , as well as a 1.38 μm reflectance test [Marchant *et al.*, 2015]. The second product, reported in Cloud_Phase_Infrared_1km and denoted here as f_2 , is a daytime and nighttime product derived from three IR window channel pairs, namely, 7.3 and 11 μm , 8.5 and 11.0 μm , and 11.0 and 12.0 μm [Baum *et al.*, 2012]. Here ice phase pixels during daytime (i.e., solar zenith angle < 81.4°) are determined for OE-IR retrievals (and MYD06) by f_1 ; for nighttime pixels, cloud phase is determined only by f_2 . Instead of using all available 1 km pixels for the aggregation, we sample every fifth pixel, which is consistent with the MYD08 sampling strategy and greatly increases computational speed without affecting the monthly gridded statistics [Oreopoulos, 2005]. The sampled 1 km pixels are aggregated globally on a 1° × 1° grid. In order to avoid artificial differences between the daytime and nighttime retrievals, all OE-IR retrievals exclude the MODIS 3.8 μm channel.

Figures 7a and 7b show the spatial distributions of the sampled single-layer ice cloud pixels during the daytime and nighttime, respectively, for May 2012. Daytime pixels are those having solar zenith angle (SZA) smaller than 81.4°. Figures 7c and 7d show the daytime and nighttime single-layer ice cloud fractions according to the two cloud phase products mentioned above. The white spots in Figure 7 (and also in Figures 8–12) indicate that there is no available data in those regions. Figure 8a shows the daytime MODIS τ and r_{eff} retrieval rate, defined as the ratio of the number of single-layer ice cloud pixels with successful MYD06 τ and r_{eff} retrievals to the total number of selected single-layer ice cloud pixels. Since C6 MYD06 always reports h if a pixel is defined as cloud, the h retrieval rates for C6 MYD06 are 100% for both daytime and nighttime (see Table 2). Figures 8b and 8c show the OE-IR retrieval rates during the daytime and nighttime, respectively. The OE-IR retrieval rate is the ratio of the number of single-layer ice cloud pixels for which the OE-IR successfully retrieves all three ice cloud properties (τ , r_{eff} , and h) to the total number of single-layer ice cloud pixels. For the OE-IR algorithm, a successful

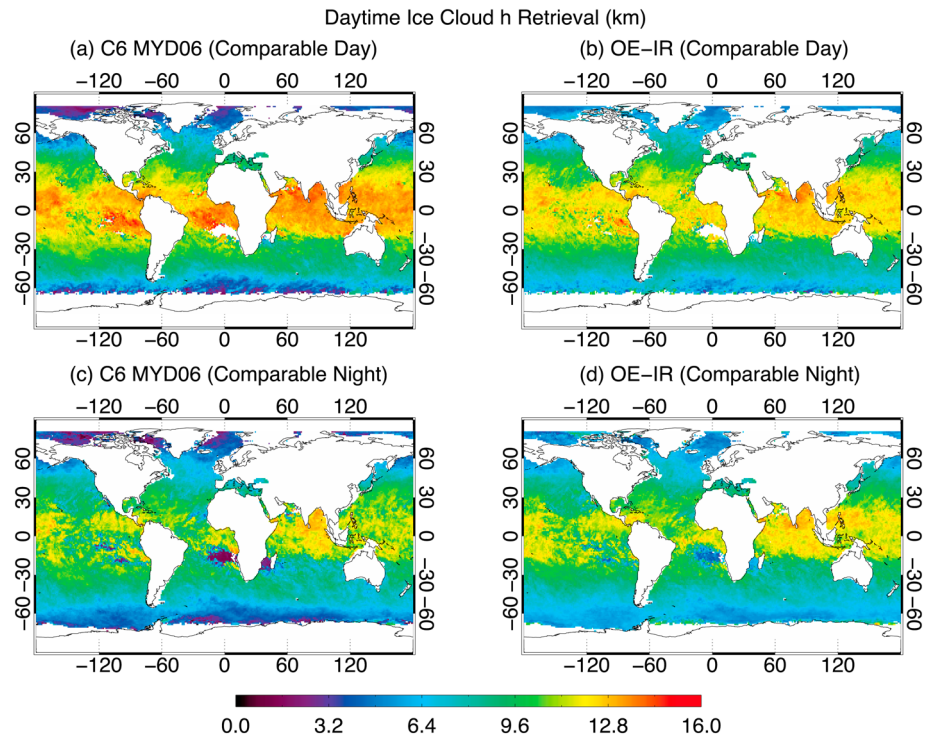


Figure 11. Comparisons of monthly h retrievals between the C6 MYD06 and OE-IR. (a, b) Comparable daytime h retrievals; (c, d) comparable nighttime h retrievals.

retrieval indicates that the retrieved cost function is smaller than 20 (see Table 2). For the month shown here, 84.8% of the total ice cloud pixels during the daytime have successful MYD06 τ and r_{eff} retrievals, which is larger than the daytime OE-IR rate of 71.6%. From Figure 8a, it is evident that the MYD06 retrieval rate decreases in regions where ice clouds have quite low fractions, in particular off the west coast of the North and South America, and southern Africa. Figures 9a and 9b show that ice clouds are optically thin in these regions, suggesting that the VNIR/SWIR retrieval is more likely to be influenced by the surface reflection and lower level clouds and aerosols, which are frequently observed in these regions. The MYD06 retrieval rate also decreases in high-latitude regions because the $\tau - r_{\text{eff}}$ pairs more frequently lie outside of the precomputed lookup table (LUT) solution space when clouds are optically thin (e.g., near ice cloud edges) and the SZAs are large (the plane-parallel approximation is no longer appropriate [Varnai and Davies, 1999]). Meanwhile, the accuracy of the cloud phase determination algorithms near the polar region may also decrease due to the low surface-cloud temperature contrast and the decreased phase sensitivity of the spectral r_{eff} tests. The retrieval rate of the daytime OE-IR algorithm is higher than that of C6 MYD06 in these special regions since the IR signal is less sensitive to the location of the cloud and the solar geometry. However, the overall OE-IR retrieval rate (71%) is lower than C6 MYD06 because of large retrieval cost functions. Large cost functions occur for multiple reasons, such as the breakdown of the plane-parallel and single-layer cloud approximation, mixed phase clouds, and large cloud optical thicknesses.

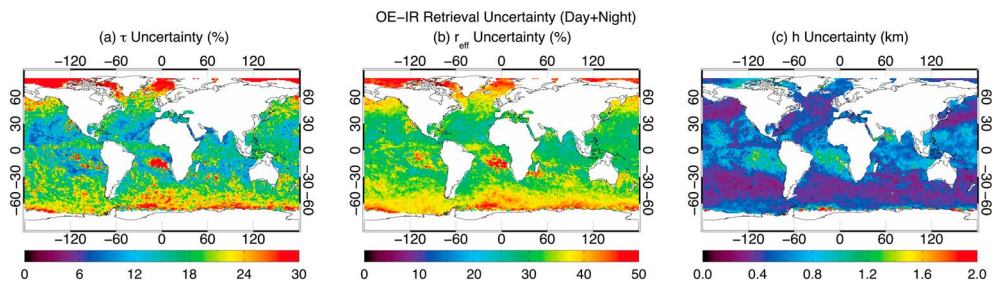


Figure 12. Monthly OE-IR retrieval uncertainties for (a) τ , (b) r_{eff} , and (c) h derived from successful OE-IR retrievals.

Table 2. Retrieval Rates of the OE-IR and the C6 MYD06 Algorithms^a

Retrieval Product		Successful Retrieval ^b		Comparable Retrieval ^c	
		τ and r_{eff}	h	τ and r_{eff}	h
OE-IR	Day	71.6%	71.6%	45.0%	71.6%
	Night	70.8%	70.8%	-	70.8%
	Total	71.1%	71.1%	15.8%	71.1%
C6 MYD06	Day	84.8%	100.0%	45.0%	71.6%
	Night	-	100.0%	-	70.8%
	Total	29.8%	100.0%	15.8%	71.1%

^aPartly cloudy and multilayered cloudy pixels are not considered.
^bSuccessful retrieval: OE-IR: Retrieval cost function < 20. C6 MYD06: Simultaneously retrieves τ and r_{eff} (or h).
^cComparable retrieval: for τ and r_{eff} : Both OE-IR and C6 MYD06 successfully retrieve τ and r_{eff} , and retrieved $\tau < 10$; for h : both C6 MYD06 and OE-IR successfully retrieve h .

For these cases, the OE-IR retrievals may have large uncertainties/biases from the cloud, surface, and other atmospheric components.

To facilitate a more appropriate retrieval comparison, constraints are applied to both the OE-IR and C6 MYD06 retrievals. Because investigating the possibility of combining the VNIR/SWIR and OE-IR retrievals is an important objective of this work, it is important to limit the retrieval comparison to portions of the τ and r_{eff} solution space in which both the OE-IR and C6 MYD06 algorithms have

sufficient sensitivity. We therefore consider an ice cloud pixel appropriate for OE-MODIS τ and r_{eff} comparison if (1) both the C6 MYD06 and OE-IR retrievals are successful and (2) the OE-IR and C6 MYD06 τ are both smaller than 10. These constraints, and the global retrieval rates for the comparable pixel subset, are summarized in Table 2. The gridded fractions of daytime ice cloud pixels for which the OE-IR and C6 MYD06 have comparable τ and r_{eff} retrievals are shown in Figure 8d. Less than half (45.0%) of the daytime ice cloud pixels are suitable for OE-IR/MYD06 τ and r_{eff} comparison. For cloud top height, comparable retrievals are defined as those for which both OE-IR and C6 MYD06 have successful h retrievals. Since the C6 MYD06 has 100% retrieval rate of h , the fraction of comparable h retrieval is identical with the OE-IR retrieval rate as shown in Figures 8b and 8bc. The C6 MYD06 and OE-IR have the same retrieval populations if the comparable retrieval constraint is applied.

Figures 9a and 9b show the monthly daytime ice cloud τ from C6 MYD06 and the OE-IR. Similar to the granule comparisons discussed in section 3, the monthly ice cloud τ distribution patterns from the two products are highly consistent. The largest discrepancy between the two occurs for optically thick cloud regions where the mean τ of C6 MYD06 is larger than 10, while the OE-IR τ is approximately 5. It is important to emphasize again that the two products are averaged here over different ice cloud populations. Optically thick ice clouds are included in the mean τ of C6 MYD06 monthly retrievals, while the OE-IR method removes some of these samples with large cost functions (larger than 20) for better quality. Figures 9c and 9d show the monthly mean τ of the C6 MYD06 and OE-IR for the comparable retrieval subset described above. Obviously, the discrepancies observed in Figures 9a and 9b significantly decrease since optically thick clouds are removed from both products. Similar comparisons of r_{eff} between the two retrievals are shown in Figure 10. In contrast to the τ comparison, there is no obvious correlation between the two products. Furthermore, the C6 MYD06 r_{eff} are systematically larger than those of OE-IR. The OE-IR r_{eff} values are around 20 μm , while the C6 MYD06 r_{eff} values are generally located between 30 and 40 μm . Further discussion about r_{eff} comparison is given at the end of this section. Figure 11 shows h comparisons for the comparable retrieval subset. The two retrievals are consistent with each other. During the daytime (Figures 11a and 11b), the C6 MYD06 h is slightly higher than OE-IR in the tropics and is lower than OE-IR in high-latitude regions. As discussed before, the OE-IR retrieval includes two water vapor channels (6.7 and 7.3 μm) in addition to the channels used in the C6 MYD06 algorithm. During the nighttime, the C6 MYD06 h decreases by 1–2 km in the tropics, possibly due to less deep convective clouds. However, very low ice cloud top heights (e.g., lower than 2 km) are found in the stratocumulus region off the west coast of southern Africa. It is quite possible that the C6 MYD06 IR phase algorithm incorrectly classifies lower level water or mixed phase clouds as ice clouds, whereas the daytime cloud optical retrieval phase performs better with the additional information content provided by SWIR observations.

Figure 12 shows the OE-IR retrieval uncertainties. On average, the OE-IR uncertainties in τ , r_{eff} , and h are 19%, 33%, and 0.48 km, respectively. The spatial distributions of τ and r_{eff} uncertainties are similar. Specifically, three large τ and r_{eff} retrieval uncertainty regions are found: (1) the storm track region and the southern oceans where convective clouds with large ice cloud optical thicknesses are frequently observed, (2) high-latitude regions where the contrast between the surface and cloud top temperatures is small, and (3) off

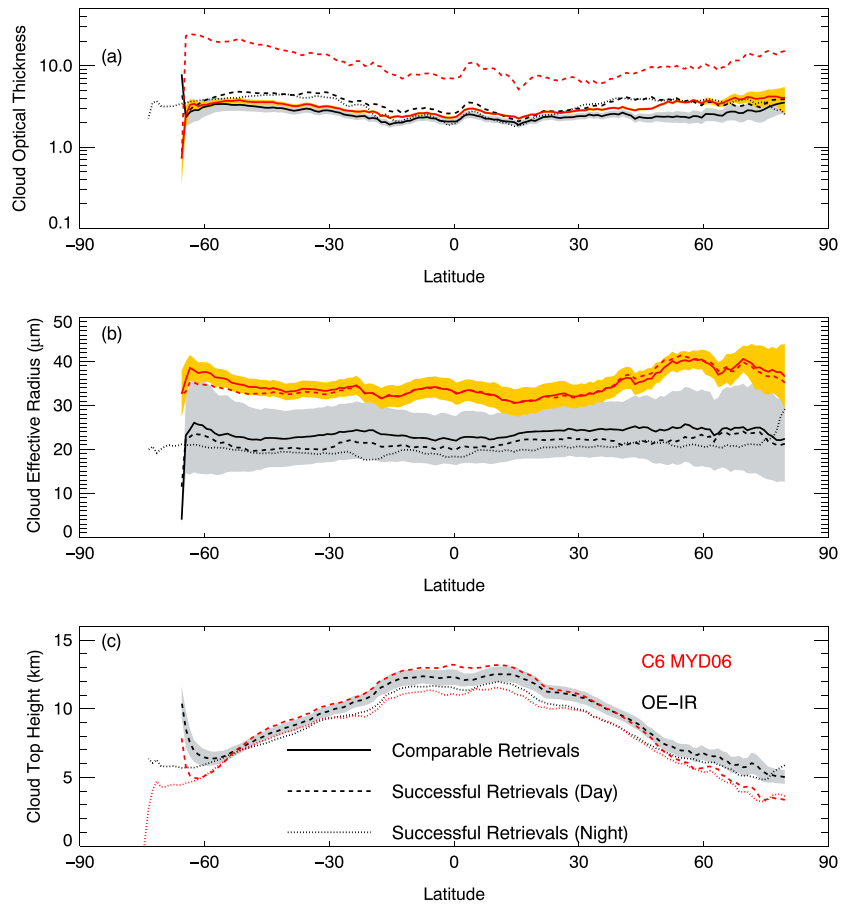


Figure 13. Comparisons of zonal mean ice cloud properties from the OE-IR (black) and C6 MYD06 (red). Solid curves indicate retrievals for comparable pixel populations (see text for details). Dashed and dotted curves indicate successful retrievals (without concern about matching pixel populations) during the daytime and nighttime, respectively. Gray and yellow shadows indicate averaged retrieval uncertainties of the OE-IR and C6 MYD06 comparable retrievals, respectively. (c) For cloud top height retrieval, solid curve is not shown because comparable h retrievals are almost identical with successful h retrievals.

the west coast of South America and Africa where only a few samples are collected and retrievals may be influenced by the persistently present marine boundary layer stratocumulus [Baum et al., 2012; King et al., 2013]. Large h uncertainty regions coincide with small τ regions. In large τ regions, the cloud top temperature is closer to the brightness temperatures in the MODIS IR window bands.

Figure 13 shows zonal mean comparisons between the C6 MYD06 and OE-IR. As expected, the MYD06 τ is approximately 3–5 times larger than the OE-IR if only independently successful retrieval filtering is used (see the red and black dashed curves in Figure 13a). However, for the comparable retrieval population, the two products are much closer to each other (solid curves in Figure 13a). From the OE-IR retrieval, the averaged daytime ice cloud τ is slightly larger than the nighttime, in particular in the tropics (see the black dashed and dotted curves in Figure 13). This day-night τ difference exists even when using the same cloud phase product, i.e., Cloud_Phase_Infrared_1km, to determine the ice cloud pixel population during both the daytime and nighttime (the result is not shown here). Comparisons of r_{eff} products are given in Figure 13b. It shows that the C6 MYD06 r_{eff} is systematically larger than the OE-IR retrievals. By applying the comparable retrieval filtering, the OE-IR r_{eff} increases slightly, and the variation pattern becomes similar to the C6 MYD06, especially in the Southern Hemisphere. It is also found that, on average, the OE-IR daytime r_{eff} is approximately 1–2 μm larger than the nighttime r_{eff} . Cloud top height comparisons are shown in Figure 13c. The curves of comparable retrievals for both C6 MYD06 and OE-IR are not shown here since they are identical to the successful retrieval curves. The averaged h difference between the two products is less than 1 km during the daytime, and the C6 MYD06 h is slightly larger than the OE-IR. During the nighttime,

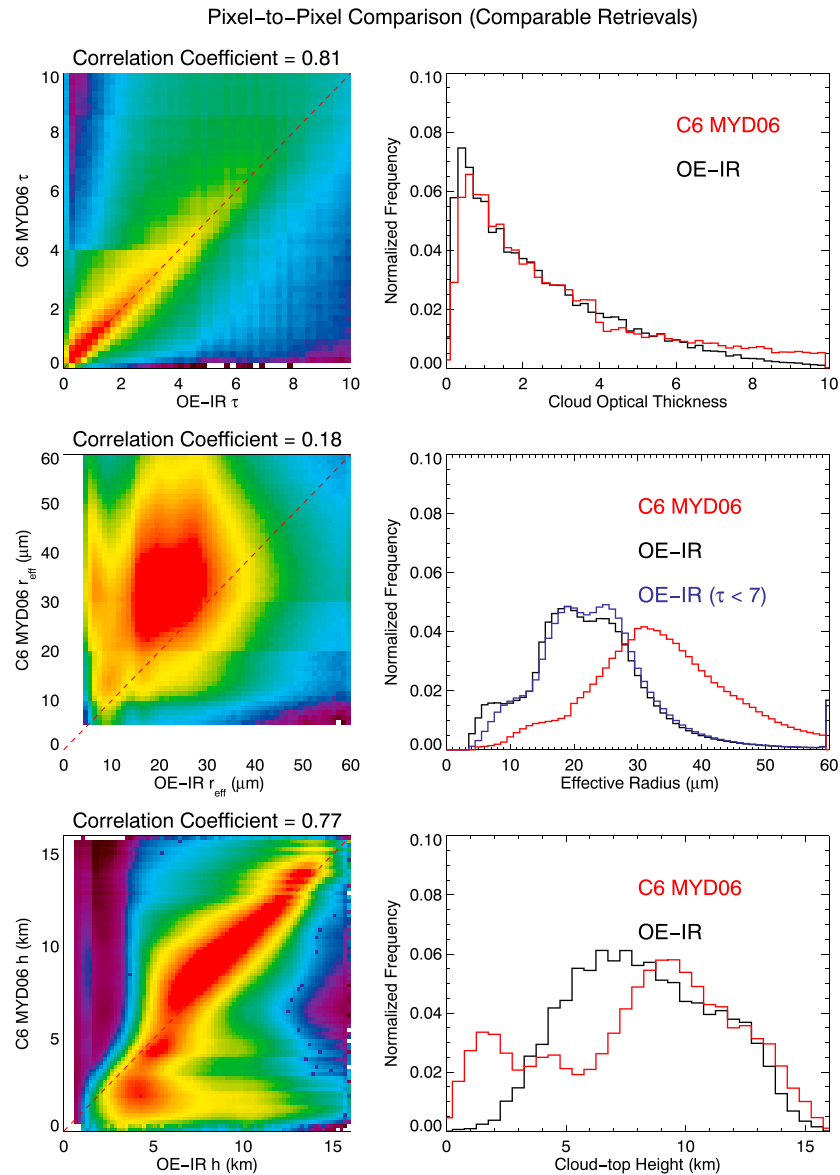


Figure 14. (left column) Scatterplots of the pixel level comparisons between the C6 MYD06 and OE-IR comparable retrievals. (right column) The probability density functions of the C6 MYD06 and OE-IR retrieved cloud properties.

both the C6 MYD06 and OE-IR have lower cloud top height retrievals. It is found that the C6 MYD06 nighttime h is 1 or 2 km lower than the OE-IR in high-latitude regions (e.g., 60–80°N/S). The OE-IR and C6 MYD06 retrieval uncertainties for comparable retrievals are also shown in Figure 13 (gray and yellow shadows).

Figure 14 shows pixel level comparisons between the C6 MYD06 and OE-IR using the 1 month comparable retrieval subset. For τ and h retrievals, the C6 MYD06 is highly correlated with OE-IR (correlation coefficients are 0.81 and 0.77, respectively), and the highest density regions (red) lie on the 1-to-1 lines. About 18% of the C6 MYD06 h retrievals are lower than 4 km and are systematically lower than the OE-IR h . From Figure 11, it is evident that these low-level clouds frequently occur in high-latitude regions. The large h discrepancies are possibly due to the presence of sea ice that is not identified by the Snow/Ice Mask (from the C6 MYD06 Cloud_Mask_1km data set). Figure 15 evaluates the OE-IR and C6 MYD06 h retrievals using CALIOP in high-latitude regions (latitude > 60°N/S). To supplement the Snow/Ice Mask, the daily Near-Real-Time Ice and Snow Extent (NISE) 25 km product [Nolin *et al.*, 1998] of the National Snow and Ice Data Center (NSIDC) is used to further screen for ice-covered surfaces.

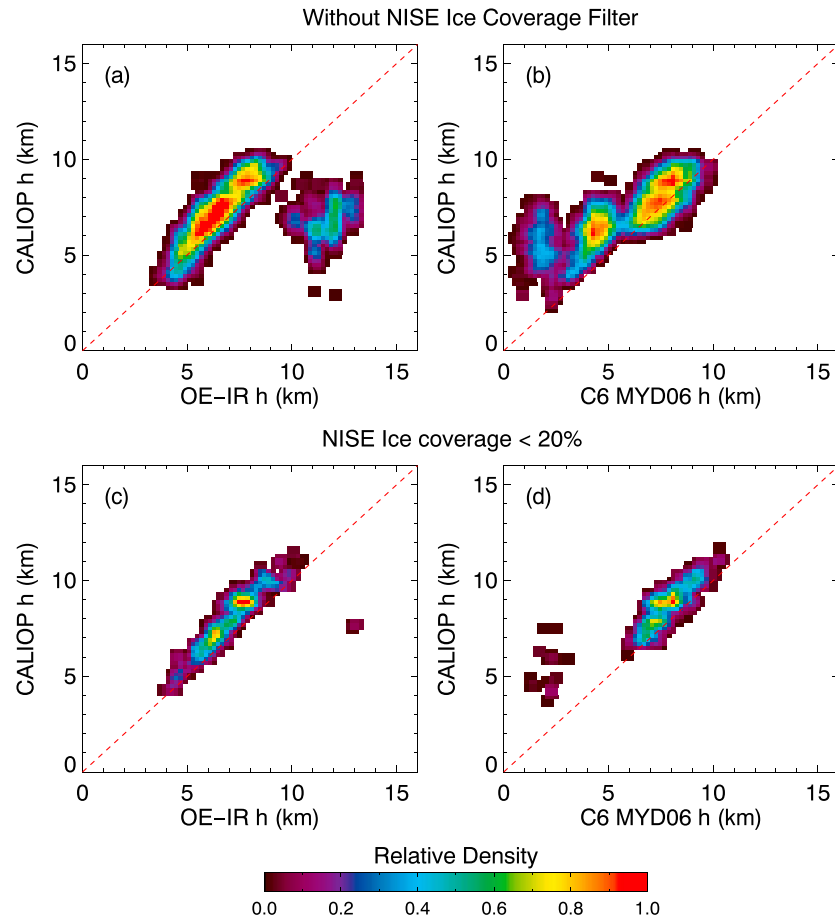


Figure 15. Scatterplots of the pixel level comparisons (a, c) between the OE-IR h and CALIOP h and (b, d) between the C6 MYD06 h and CALIOP h for comparable retrievals along the CALIPSO track. Figures 15a and 15b show comparisons without applying the Near-Real-Time Ice and Snow Extent (NISE) ice coverage filter; Figures 15c and 15d show comparisons with the NISE ice coverage $< 20\%$ filter.

Comparisons without using the NISE sea ice coverage filter are shown in Figure 15a and 15b. It is interesting to find that, without the NISE sea ice coverage filter, a fraction of OE-IR (or C6 MYD06) retrievals has higher (or lower) h than CALIOP. The OE-IR always uses nine MODIS IR bands (bands 27–36, except band 30), but the C6 MYD06 uses only the 11 μm band to derive h for clouds with cloud top pressure greater than 600 hPa or when the CO₂-slicing algorithm is unable to produce reasonable retrievals [Baum *et al.*, 2012]. This implies that the use of different channels may bias the two retrievals in different directions. Comparisons with the NISE sea ice coverage filter (i.e., pixels with ice coverage $< 20\%$) are shown in Figures 15c and 15d. The biased retrievals from both OE-IR and C6 MYD06 are generally removed, suggesting that the large h biases may be caused by the presence of underlying sea ice.

For the cloud r_{eff} comparison shown in Figure 14 (middle row), the correlation coefficient (0.18) of the C6 MYD06 and OE-IR r_{eff} products is small. The C6 MYD06 r_{eff} has a Gaussian-like distribution with a mode at 32 μm and a wider standard deviation of approximately 10 μm . The OE-IR r_{eff} distribution, however, has two modes at 7 and 19 μm . It is possible that the mode at small r_{eff} is caused by the limitation of the OE-IR retrieval that r_{eff} becomes unstable if τ is large. Figure 14b shows that the 7 μm mode disappears if cloud pixels with C6 MYD06 and OE-IR retrieved $\tau < 7$ are used for comparison. Ultimately, it is difficult to explain the r_{eff} differences between the two retrievals. It should be noted that Heidinger *et al.* [2015] derived an empirical ice crystal model from MODIS IR observations, defined at pixel level as the ice crystal habit that provides the best spectral consistency between r_{eff} retrieved from 11–12 μm and 11–8.5 μm β ratios, that reduces the r_{eff} inconsistency between the IR and VNIR/SWIR/MWIR methods. Another possible reason is that

the C6 MYD06 cloud particle size information shown here is inferred from the 2.1 μm reflectance, which may contain signal reflected by lower parts of a cloud [Zhang *et al.*, 2009]. The IR signal, on the other hand, may only include emission from the uppermost part of the cloud. Therefore, a large r_{eff} difference could be found if the ice cloud is vertically inhomogeneous [Zhang *et al.*, 2010]. Zhang *et al.* [2010] also showed that the difference varies with ice cloud optical thickness and vertical distributions of cloud particle size. Meanwhile, multilayered clouds and cloud 3-D effects can also introduce large uncertainties. Further investigation is required to understand the large r_{eff} retrieval differences.

5. Summary and Conclusion

The MODIS imagers onboard the Terra and Aqua satellites, with moderate spatial resolution and wide spectral coverage, have collectively monitored global ice clouds for more than 13 years. However, the operational cloud optical and microphysical property retrievals from MODIS (MYD06 for Aqua MODIS) are only available during the daytime since the retrieval algorithm is based on VNIR/SWIR/MWIR observations. Such approaches that rely on solar window channels are known to have decreased sensitivity to optically thin clouds, and the retrievals of these clouds can have large uncertainties. In order to supplement the current MYD06 cloud optical and microphysical property retrievals of optically thin ice clouds, and to help fill the data gap during nighttime, we have developed an infrared optimal estimation (OE-IR)-based ice cloud retrieval algorithm (Part 1) and conducted comprehensive comparisons here between the OE-IR and Collection 6 (C6) MYD06 retrievals. The OE-IR algorithm provides quantitative pixel level retrieval error estimation including contributions from measurement uncertainty, forward model uncertainty, atmospheric profile parameter uncertainty, and preassumed ice crystal habit uncertainty. With the exception of the last error source, a similar uncertainty analysis is given in C6 MYD06 product.

Different from the C6 MYD06 algorithm, the OE-IR retrieval uses infrared observations in multiple spectral channels from 6.7 to 15 μm to simultaneously infer ice cloud optical thickness (τ), effective radius (r_{eff}), and cloud top height (h). The inherent advantage of the OE-IR retrieval is that it is independent of solar geometry and less dependent on satellite viewing angles. Using forward model simulations, it is shown that the OE-IR retrieval performs best when ice cloud τ is between 0.5 and 7. We compare the two retrievals using both case studies and monthly statistics (May 2012). It is found that the OE-IR retrieved τ values are closer to the lidar in optically thin ice cloud regions (e.g., $\tau < 1$), compared with the MYD06 retrieval that has a high failure rate in regions where clouds are optically thin. For moderately optically thick ice clouds (e.g., $1 < \tau < 7$), the MYD06 retrieved τ are highly consistent with the OE-IR, while MYD06 τ becomes systematically larger than OE-IR for optically thick clouds ($\tau > 7$). Generally, the OE-IR and MYD06 retrievals are comparable and consistent, in particular for τ and h . Relatively large h differences occur in high-latitude regions, due in part to sea ice contamination. The correlation coefficient of τ and h from the two retrievals is 0.81 and 0.77, respectively, when $\tau < 10$. For r_{eff} , while a weak positive correlation coefficient (0.18) is found between the two retrievals, large differences are observed. This large r_{eff} retrieval discrepancy may be caused by ice cloud vertical or horizontal inhomogeneity, multilayer clouds, or cloud 3-D effects [Iwabuchi and Hayasaka, 2002; Marshak *et al.*, 2006; Fauchez *et al.*, 2014, 2015; Cornet *et al.*, 2005], all of which may reduce retrieval accuracy since both retrievals assume simplified one-dimensional single-layer ice clouds. Further investigation is needed to fully understand the differences between the IR and VNIR/SWIR r_{eff} retrievals and to improve retrieval algorithms in the future.

While the OE-IR retrieval results shown here are only from Aqua MODIS, the algorithm can be applied to any sensor having the necessary IR channels, including narrow-band geosynchronous imagers such as ABI and SEVIRI, as well as hyperspectral polar orbiting sensors such as CrIS, IASI (Infrared Atmospheric Sounding Interferometer) [Blumstein *et al.*, 2004], and AIRS. Consistent daytime and nighttime retrievals allow for samples of the diurnal cycle of global ice clouds. As the MODIS IR observations are sensitive to the optical properties of thin cirrus, the present OE-IR-based τ and h products are complementary to the widely used VNIR/SWIR/MWIR τ and CO_2 slicing h retrieval algorithms. Furthermore, improving the radiative transfer and ice crystal habit models may reduce the large r_{eff} discrepancies between the C6 MYD06 and OE-IR products. By combining the OE-IR and VNIR/SWIR retrievals, a more complete ice cloud property retrieval product can be created, providing better observations for understanding cloud properties and constraining dynamical models.

Acknowledgments

The authors are grateful for support from the NASA Radiation Sciences Program. Chenxi Wang would like to thank Qianhua Liu, David Groff, and Eva E. Borbas for their help on CRTM. The computations in this study were performed on the UMBC High Performance Computing Facility (HPCF); this facility is supported by the U.S. National Science Foundation through the MRI program (grant CNS-0821258 and CNS-1228778) and the SCREMS program (grant DMS 0821311), with additional substantial support from UMBC. The Collection 6 MODIS and CALIPSO/CALIOP products are publicly available at NASA/LAADS (<ftp://ladsweb.nascom.nasa.gov/allData/6/>) and NASA/ASDC (<https://eosweb.larc.nasa.gov/>).

References

- Aminou, D. (2002), MSG's SEVIRI instrument, *ESA Bull.*, *111*, 15–17.
- Aumann, H. H., et al. (2003), AIRS/AMSU/HSB on the Aqua mission: Design, science objectives, data products and processing system, *IEEE Trans. Geosci. Remote Sens.*, *41*, 253–264.
- Austin, R. T., A. J. Heymsfield, and G. L. Stephens (2009), Retrieval of ice cloud microphysical parameters using the CloudSat millimeter-wave radar and temperature, *J. Geophys. Res.*, *114*, D00A23, doi:10.1029/2008JD010049.
- Baran, A. J., and P. N. Francis (2004), On the radiative properties of cirrus cloud at solar and thermal wavelengths: A test of model consistency using high resolution airborne radiance measurements, *Q. J. R. Meteorol. Soc.*, *130*, 763–778.
- Barnes, W. L., T. S. Pagano, and V. V. Salomonson (1998), Prelaunch characteristics of the Moderate Resolution Imaging Spectroradiometer (MODIS) on EOS-AM1, *IEEE Trans. Geosci. Remote Sens.*, *36*, 1088–1100.
- Baum, B. A., W. P. Menzel, R. A. Frey, D. C. Tobin, R. E. Holz, and S. A. Ackerman (2012), MODIS cloud-top property refinements for Collection 6, *J. Appl. Meteorol. Climatol.*, *51*, 1145–1163, doi:10.1175/JAMC-D-11-0203.1.
- Baum, B. A., P. Yang, A. J. Heymsfield, A. Bansemir, B. H. Cole, A. Merrelli, C. Schmitt, and C. Wang (2014), Ice cloud single-scattering property models with the full phase matrix at wavelengths from 0.2 to 100 μm , *J. Quant. Spectrosc. Radiat. Transfer*, *146*, 123–139.
- Blumstein, D., et al. (2004), IASI instrument: Technical overview and measured performances, in *Infrared Spaceborne Remote Sensing XII*, vol. 5543, edited by M. Strojnik, pp. 196–207, Intl. Soc. for Opt. Eng., Denver, Colo.
- Boucher, O., et al. (2013), Clouds and aerosols, in *Climate Change 2013: The Physical Science Basis. Contribution of Working Group I to the Fifth Assessment Report of the Intergovernmental Panel on Climate Change*, edited by T. F. Stocker et al., Cambridge Univ. Press, Cambridge, U. K., and New York.
- Chepfer, H., G. Brogniez, and Y. Fouquart (1998), Cirrus clouds' microphysical properties deduced from POLDER observations, *J. Quant. Spectrosc. Radiat. Transfer*, *60*, 375–390.
- Clough, S. A., M. W. Shephard, E. J. Mlawer, J. S. Delamere, M. J. Iacono, K. Cady-Pereira, S. Boukabara, and P. D. Brown (2005), Atmospheric radiative transfer modeling: A summary of the AER codes, *J. Quant. Spectrosc. Radiat. Transfer*, *91*, 233–244.
- Cole, B. H., P. Yang, B. A. Baum, J. Riedi, L. C.-Labonnote, F. Thieuleux, and S. Platnick (2013), Comparison of PARASOL observations with polarized reflectances simulated using different ice habit mixtures, *J. Appl. Meteorol. Climatol.*, *52*, 186–196.
- Cooper, S., and T. J. Garrett (2010), Identification of small ice cloud particles using passive radiometric observations, *J. Appl. Meteorol. Climatol.*, *49*, 2334–2347.
- Cornet, C., J. C. Buriez, J. Riedi, H. Isaka, and B. Guillemet (2005), Case study of inhomogeneous cloud parameter retrieval from MODIS data, *Geophys. Res. Lett.*, *32*, L13807, doi:10.1029/2005GL022791.
- Eliasson, S., S. A. Buehler, M. Milz, P. Eriksson, and V. O. John (2011), Assessing observed and modelled spatial distributions of ice water path using satellite data, *Atmos. Chem. Phys.*, *11*, 375–391, doi:10.5194/acp-11-375-2011.
- Eliasson, S., G. Holl, S. A. Buehler, T. Kuhn, M. Stengel, F. Iturbide-Sanchez, and M. Johnston (2013), Systematic and random errors between collocated satellite ice water path observations, *J. Geophys. Res. Atmos.*, *118*, 2629–2642, doi:10.1029/2012JD018381.
- Faucheux, T., C. Cornet, F. Szczap, P. Dubuisson, and T. Rosambert (2014), Impact of cirrus clouds heterogeneities on top-of-atmosphere thermal infrared radiations, *Atmos. Chem. Phys.*, *14*, 5599–5615.
- Faucheux, T., P. Dubuisson, C. Cornet, F. Szczap, A. Garnier, J. Pelon, and K. Meyer (2015), Impacts of cloud heterogeneities on cirrus optical properties retrieved from space-based thermal infrared radiometry, *Atmos. Meas. Tech.*, *8*, 633–647.
- Garnier, A., J. Pelon, P. Dubuisson, M. Faivre, O. Chomette, N. Pascal, and D. P. Kratz (2012), Retrieval of cloud properties using CALIPSO Imaging Infrared Radiometer. Part I: Effective emissivity and optical depth, *J. Appl. Meteorol. Climatol.*, *51*, 1407–1425.
- Garnier, A., et al. (2013), Retrieval of cloud properties using CALIPSO Imaging Infrared Radiometer. Part II: Effective diameter and ice water path, *J. Appl. Meteorol. Climatol.*, *52*, 2582–2599.
- Han, Y., et al. (2013), Suomi NPP CrIS measurements, sensor data record algorithm, calibration and validation activities, and record data quality, *J. Geophys. Res. Atmos.*, *118*, 1–15, doi:10.1002/2013JD020344.
- Heidinger, A. K., Y. Li, B. A. Baum, R. E. Holz, S. Platnick, and P. Yang (2015), Retrieval of cirrus cloud optical depth under day and night conditions from MODIS Collection 6 cloud property data, *Remote Sens.*, *7*, 7257–7271, doi:10.3390/rs70607257.
- Holl, G., S. Eliasson, J. Mendrok, and S. A. Buehler (2013), SPARE-ICE: Synergistic ice water path from passive operational sensors, *J. Geophys. Res. Atmos.*, *119*, 1504–1523, doi:10.1002/2013JD020759.
- Holz, R. E., S. A. Ackerman, F. W. Nagle, R. Frey, S. Dutcher, R. E. Kuehn, M. A. Vaughan, and B. Baum (2008), Global Moderate Resolution Imaging Spectroradiometer (MODIS) cloud detection and height evaluation using CALIOP, *J. Geophys. Res.*, *113*, D00A19, doi:10.1029/2008JD009837.
- Holz, R. E., et al. (2015), Resolving cirrus optical thickness biases between CALIOP and MODIS using infrared retrievals, *Atmos. Chem. Phys. Discuss.*, *15*, 29,455–29,495, doi:10.5194/acpd-15-29455-2015.
- Iwabuchi, H., and T. Hayasaka (2002), Effects of cloud horizontal inhomogeneity on the optical thickness retrieved from moderate-resolution satellite data, *J. Atmos. Sci.*, *59*, 2227–2242.
- Kahn, B. H., et al. (2008), Cloud type comparisons of AIRS, CloudSat, and CALIPSO cloud height and amount, *Atmos. Chem. Phys.*, *8*, 1231–1248.
- Kahn, B. H., et al. (2014), The Atmospheric Infrared Sounder version 6 cloud products, *Atmos. Chem. Phys.*, *14*(1), 399–426, doi:10.5194/acp-14-399-2014.
- King, M. D., S. Platnick, W. P. Menzel, S. A. Ackerman, and P. A. Hubanks (2013), Spatial and temporal distribution of clouds observed by MODIS onboard the Terra and Aqua satellites, *IEEE Trans. Geosci. Remote Sens.*, *51*, 3826–3852.
- Lebsock, M., and H. Su (2014), Application of active spaceborne remote sensing for understanding biases between passive cloud water path retrievals, *J. Geophys. Res. Atmos.*, *119*, 8962–8979, doi:10.1002/2014JD021568.
- Li, J. L. F., D. Waliser, C. Woods, J. Teixeira, J. Bacmeister, J. Chern, B. W. Shen, A. Tompkins, W. K. Tao, and M. Kohler (2008), Comparisons of satellites liquid water estimates with ECMWF and GMAO analyses, 20th century IPCC AR4 climate simulations, and GCM simulations, *Geophys. Res. Lett.*, *35*, L19710, doi:10.1029/2008GL035427.
- Marchant, B., S. Platnick, K. Meyer, G. T. Arnold, and J. Riedi (2015), MODIS Collection 6 shortwave-derived cloud phase classification algorithm and comparisons with CALIOP, *Atmos. Meas. Tech. Discuss.*, *8*, 11,893–11,924, doi:10.5194/amtd-8-11893-2015.
- Marshak, A., J. V. Martins, V. Zubko, and Y. J. Kaufman (2006), What does reflection from cloud sides tell us about vertical distribution of cloud droplet sizes, *Atmos. Chem. Phys.*, *6*, 5295–5305.
- McClatchey, R. A., R. W. Fenn, J. E. A. Salby, F. E. Volz, and J. S. Garing (1972), Optical properties of the atmosphere. Air Force Cambridge Res. Lab. Tech. Rep. AFCRL-72-0497, 108 pp.

- Menzel, W. P., R. A. Frey, H. Zhang, D. P. Wylie, C. C. Moeller, R. E. Holz, B. Maddux, B. A. Baum, K. I. Strabala, and L. E. Gumley (2008), MODIS global cloud-top pressure and amount estimation: Algorithm description and results, *J. Appl. Meteorol. Climatol.*, *47*, 1175–1198, doi:10.1175/2007JAMC1705.1.
- Minnis, P., et al. (2011), CERES edition-2 cloud property retrievals using TRMM VIRS and TERRA and AQUA MODIS data, part I: Algorithms, *IEEE Trans. Geosci. Remote Sens.*, *49*, 4374–4400.
- Nakajima, T., and M. D. King (1990), Determination of the optical thickness and effective particle radius of clouds from reflected solar radiation measurements. Part I: Theory, *J. Atmos. Sci.*, *47*, 1878–1893.
- Nolin, A., R. L. Armstrong, and J. Maslanik (1998), Near-real-time SSM/I-SSMIS EASE-grid daily global ice concentration and snow extent, version 4 (2001–2013), NASA DAAC at the National Snow and Ice Data Center, Boulder, Colo.
- Oreopoulos, L. (2005), The impact of subsampling on MODIS level-3 statistics of cloud optical thickness and effective radius, *IEEE Trans. Geosci. Remote Sens.*, *43*, 366–373.
- Parol, F., J. C. Buriez, G. Brogniez, and Y. Fouquart (1991), Information content of AVHRR channels 4 and 5 with respect to the effective radius of cirrus cloud particles, *J. Appl. Meteorol.*, *30*, 973–984.
- Platnick, S., M. D. King, S. A. Ackerman, W. P. Menzel, B. A. Baum, J. C. Riedi, and R. A. Frey (2003), The MODIS cloud products: Algorithms and examples from Terra, *IEEE Trans. Geosci. Remote Sens.*, *41*, 459–473, doi:10.1109/TGRS.2002.808301.
- Platnick, S., et al. (2013), MODIS cloud optical properties: User guide for the Collection 6 level-2 MOD06/MYD06 product and associated level-3 datasets, MODIS MOD06 User Guide.
- Platnick, S., et al. (2015), MODIS Atmosphere L2 Cloud Product (06_L2). NASA MODIS Adaptive Processing System, Goddard Space Flight Center, USA, doi:10.5067/MODIS/MYD06_L2.006.
- Schmit, T. J., M. M. Gunshor, W. P. Menzel, J. Gurka, J. Li, and S. Bachmeier (2005), Introducing the next-generation advanced baseline imager (ABI) on GOES-R, *Bull. Am. Meteorol. Soc.*, *86*, 1079–1096, doi:10.1175/BAMS-86-8-1079.
- Smith, W. L., and C. M. R. Platt (1978), Comparison of satellite-deduced cloud heights with indications from radiosonde and ground-based laser measurements, *J. Appl. Meteorol.*, *17*, 1796–1802.
- Stamnes, K., S. C. Tsay, W. Wiscombe, and K. Jayaweera (1988), Numerically stable algorithm for discrete-ordinate-method, *Appl. Opt.*, *27*, 2502–2509.
- Varnai, T., and R. Davies (1999), Effects of cloud heterogeneities on shortwave radiation: Comparison of cloud-top variability and internal heterogeneity, *J. Atmos. Sci.*, *56*, 4206–4224.
- Waliser, D. E., et al. (2009), Cloud ice: A climate model challenge with signs and expectations of progress, *J. Geophys. Res.*, *114*, D00A21, doi:10.1029/2008JD010015.
- Wang, C., P. Yang, B. A. Baum, S. Platnick, A. K. Heidinger, Y. Hu, and R. E. Holz (2011), Retrieval of ice cloud optical thickness and effective particle size using a fast infrared radiative transfer model, *J. Appl. Meteorol. Climatol.*, *50*, 2283–2297, doi:10.1175/JAMC-D-11-067.1.
- Wang, C., S. Platnick, Z. Zhang, K. Meyer, and P. Yang (2016), Retrieval of ice cloud properties using an optimal estimation algorithm and MODIS infrared observations: 1. Forward model, error analysis, and information content, *J. Geophys. Res. Atmos.*, *121*, doi:10.1002/2015JD024526.
- Wind, G., S. Platnick, M. D. King, P. A. Hubanks, M. J. Pavolonis, A. K. Heidinger, P. Yang, and B. A. Baum (2010), Multilayer cloud detection with the MODIS near-infrared water vapor absorption band, *J. Appl. Meteorol. Climatol.*, *49*, 2315–2333.
- Winker, D. M., et al. (2010), The CALIPSO mission: A global 3D view of aerosols and clouds, *Bull. Am. Meteorol. Soc.*, *91*, 1211–1229.
- Wood, R. (2012), Stratocumulus clouds, *Mon. Weather Rev.*, *140*, 2373–2423, doi:10.1175/MWR-D-11-00121.1.
- Yang, P., L. Bei, B. A. Baum, K.-N. Liou, G. W. Kattawar, M. I. Mishchenko, and B. Cole (2013), Spectrally consistent scattering, absorption, and polarization properties of atmospheric ice crystals at wavelengths from 0.2 to 100 μm , *J. Atmos. Sci.*, *70*, 330–347, doi:10.1175/JAS-D-12-039.1.
- Zhang, Z., P. Yang, G. W. Kattawar, J. Riedi, L. C. Labonnote, B. A. Baum, S. Platnick, and H. L. Huang (2009), Influence of ice particle model on satellite ice cloud retrieval: Lessons learned from MODIS and POLDER cloud product comparison, *Atmos. Chem. Phys.*, *9*, 2034–2050.
- Zhang, Z., S. Platnick, P. Yang, A. K. Heidinger, and J. M. Comstock (2010), Effects of ice particle size vertical inhomogeneity on the passive remote sensing of ice clouds, *J. Geophys. Res.*, *115*, D17203, doi:10.1029/2010JD013835.